Journal of Power Sources 489 (2021) 229439

Contents lists available at ScienceDirect

Journal of Power Sources

journal homepage: www.elsevier.com/locate/jpowsour

Scaleup and manufacturability of symmetric-structured metal-supported solid oxide fuel cells

Emir Dogdibegovic, Yuan Cheng, Fengyu Shen, Ruofan Wang, Boxun Hu, Michael C. Tucker *

Energy Conversion Group, Lawrence Berkeley National Laboratory, Berkeley, CA, 94720, USA

HIGHLIGHTS

- MS-SOFCs are scaled up to 50 cm^2.
- Molten salt is replaced by a shelf-stable, sprayable liquid infiltration precursor.
- Infiltration cycle time is reduced by using a very fast heat-up.
- Active area of the cells is analyzed and corrected.

ARTICLE INFO

Keywords:
Metal-supported
SOFC
Scale up
Infiltration

ABSTRACT

Metal-supported solid oxide fuel cells with symmetric architecture, having metal supports on both sides of the cell, are scaled up from button cell size to large 50 cm^2 active area cell size. The cells remain flat after sintering assisted by the symmetric structure. Equivalent performance is achieved for button cells and large cells, and thermal cycling and redox cycling tolerance are demonstrated for the large cells. The catalyst infiltration process is improved to enable high-throughput manufacturing. The cumbersome lab-scale molten nitrate infiltration process is replaced with a room-temperature process in which a shelf-stable aqueous solution of nitrate salts is applied to the cell by spraying, painting, or other scalable techniques. A fast-ramp thermal conversion of the nitrate salts to the final oxide catalyst composition is implemented, allowing many infiltration cycles to be accomplished in a single work shift. Increasing the number of infiltration cycles from 5 to 10 led to an increase in peak power density from approximately 0.3 to 0.52 W cm^{-2}.

1. Introduction

Metal-supported solid oxide fuel cells (MS-SOFCs) and electrolysis cells (MS-SOECs) offer advantages over conventional electrode- or electrolyte-supported solid oxide fuel cells (SOFCs), including thermal cycling and redox cycling tolerance, low cost of the support material, and mechanical strength [1–4]. MS-SOCs (MS-SOFC and MS-SOECs) are being developed by many research groups globally, and commercialized by Ceres Power [2–6]. There exist various approaches for MS-SOC cell fabrication, including deposition of electrodes and electrolyte onto a pre-formed metal support using pulsed laser deposition [7,8], plasma spray [9,10], sputtering [11], or colloidal processes [5], or *via* co-sintering of the metal support and other layers produced by tape-casting and other powder slurry techniques [12–14].

It is common practice to develop new MS-SOC cell materials, cell architectures, and fabrication techniques using small "button" cells and lab-scale processes. Prior to commercialization, button cells must be scaled up to larger cell size, and lab-scale processes must be replaced with high-throughput, low-cost scalable processing techniques. The details of scale-up are specific to the MS-SOC materials and fabrication processes used by each group. A number of MS-SOFC technologies with stainless steel supports have been demonstrated at intermediate (~25 cm^2) or large cell size (up to 300 cm^2 for a single cell), and have been summarized in review articles [2,3]. Multi-cell MS-SOFC stacks have also been demonstrated [2]. For example, a 3-cell stack of MS-SOFCs with 80 cm^2 active area and 120 cm^2 cell area was subjected to rapid thermal cycling with thermal gradients around 30 °C cm^{-1} [15]. Ceres Power is commercializing 1 kW and 5 kW MS-SOFC stacks, and has reported more than 4500 h lifetime with aggressive emergency stop and thermal cycling demonstrations [5]. For steam electrolysis, MS-SOECs

* Corresponding author. LBNL, 1 Cyclotron Rd, MS 62-203, Berkeley, CA, 94720, USA.
E-mail address: mctucker@lbl.gov (M.C. Tucker).

https://doi.org/10.1016/j.jpowsour.2020.229439
Received 19 October 2020; Received in revised form 3 December 2020; Accepted 28 December 2020
Available online 20 January 2021
0378-7753/

have been demonstrated with 12.5 cm^2 active area with electrolyte applied by plasma spray [16] and with 16 cm^2 by physical vapor deposition (PVD) [17].

Lawrence Berkeley National Laboratory (LBNL) previously developed co-sintered metal-supported SOFCs (MS-SOFC) using button cells with 5–8 cm^2 area, and a slow catalyst infiltration technique using molten nitrate salts [18–24]. The LBNL MS-SOFC cell architecture is produced *via* scalable processes such as tape casting, lamination, and co-sintering which are routinely used in the ceramics industry at high manufacturing volumes. The cell consists of a symmetric structure of metal supports and zirconia electrode scaffold and electrolyte layers, Fig. 1. The symmetric structure provides for a very strong cell structure, and enables welded electrical connections on both sides of the cell. These layers are co-sintered in reducing atmosphere, followed by infiltration of catalyst precursors which are then converted to the final catalyst composition by firing in air. Here, we demonstrate much larger cell size (50 cm^2) and improved high-throughput infiltration techniques that are anticipated to be scalable to a manufacturing environment.

2. Experimental

2.1. Cell preparation

Green cells were prepared by tapecasting and laminating layers of P434L stainless steel powder (Ametek, USA) and 10Sc1Ce-doped zirconia (DKKK, Japan) with poreformer in the metal and ceramic electrode backbone, as described previously [20,21]. Individual cells were cut from a larger laminate using a laser cutter (Full Spectrum Laser), debinded in air at 525 °C, and sintered in 2% H_2/98% Ar at 1350 °C. Button cells were 19.5 mm O.D ("3 cm^2") or 32 mm O.D. ("8 cm^2"). Large rectangular cells were 65 × 80 mm with rounded corners ("50 cm^2"). After sintering, the cells were fired in air at 850 °C for 10 h to pre-oxidize the stainless steel [19]. Pr-oxide (Pr_6O_{11}) cathode and 20% Sm-doped ceria/Ni (SDCN, 60/40 vol%) anode catalysts were then applied to the cell by infiltration. The edge of the cell was masked with acrylic paint (Liquitex) to prevent catalyst deposition on the electrolyte and metal support in the perimeter area that would later be covered by glass seal, in order to prevent a catalyst short-circuit pathway across the electrolyte edge and to have uncoated metal in contact with the glass seal. Some cells were infiltrated using a standard molten salt process, discussed in detail previously [20,21,23]. Briefly, Pr-nitrate or stoichiometric mixtures of Ni-, Sm-, and Ce-nitrates (Sigma Aldrich) were melted and mixed with Triton-X surfactant and a small amount of water at ~90 °C. The cell was submerged in the nitrate melt and vacuum was applied to remove air from the pores. Other cells were infiltrated with an aqueous solution containing more water, such that the nitrate salts dissolved completely at room temperature resulting in a metal ion concentration of approximately 3.2 M (Ce, Sm, Ni) or 3.5 M (Pr). The metal ion concentrations were determined by carefully measuring the weight of metal nitrate and the total volume of the final solution in which the metal was dissolved. This solution was sprayed or dripped onto the surface of the cell, followed by application of vacuum. After infiltration of the nitrate precursor liquids, the nitrate salts were converted to Pr-oxide or SDCN-oxide by firing in air (Ni oxide is converted to Ni metal during cell operation with hydrogen fuel). In the standard "slow" firing, the cells were placed in a cold furnace and heated to the final conversion temperature with a 3 °C min^{-1} ramp rate. Cells were heated to 850 °C on the first infiltration cycle, and 600 °C on subsequent cycles [21]. For "fast" firing, a furnace was preheated to 500 °C and the cells were placed directly in the hot furnace for 10 min, and then removed from the furnace and cooled naturally in air. In both cases, the number of infiltration cycles is indicated in the text and figures.

2.2. Cell testing

Button cell and large format (65 × 80 mm) cells were mounted onto 410 stainless steel test rigs. The large test rig had cross-flow of air and fuel through straight flow channels, Fig. S1. Pt mesh was spot welded to each side of the cells to make electrical connections to the potentiostat. Glass powder was applied as a paste (Schott GM31107 mixed with terpineol) by syringe to the edges of the cells, and heated to 700 °C in air in a furnace to form the edge seal. The anode was then flushed with nitrogen before introducing humidified hydrogen (3% moisture) fuel flow. Button cells were exposed to ambient air on the cathode side and 150 cm^3 min^{-1} fuel flow on the anode side. The large cells had 3 L min^{-1} air flow and 400 cm^3 min^{-1} fuel flow. Open circuit voltage, electrochemical impedance spectroscopy at open circuit (EIS), and polarization performance were assessed with a potentiostat with current boosters (Biologic VMP3 or SP150 with 10A booster or FlexP 0012 booster).

Thermal cycling of a 50 cm^2 cell was accomplished by heating the cell and test rig in a box furnace to 700 °C, holding until the temperature equilibrated, and cooling to <100 °C. The heating rate was limited by the thermal mass of the test rig; although the furnace heated up at 40 °C min^{-1}, the cell heating rate was approximately 20 °C min^{-1}. Redox cycling was accomplished by switching the anode side gas flow cyclically between humidified hydrogen/nitrogen/air/nitrogen. Each gas was held for several minutes, and the Ni oxidation and reduction reactions occur within seconds for this infiltrated anode design [22].

2.3. Characterization

Microtomography was conducted at the Advanced Light Source (ALS) Beamline 8.3.2 at Lawrence Berkeley National Laboratory, with pixel size of 0.65 μm. Images were collected over 180° in 0.072° steps,

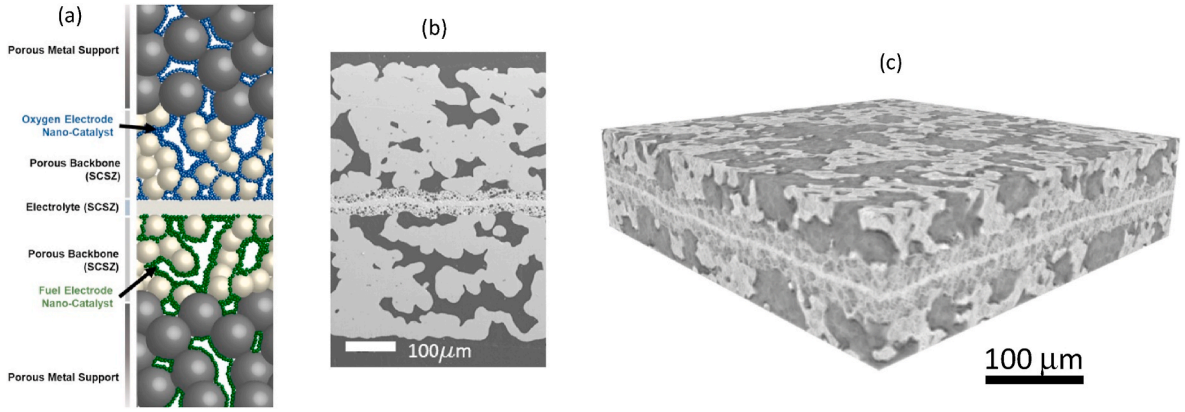

Fig. 1. MS-SOFC structure. (a) Schematic representation, (b) SEM image of polished cross section, and (c) X-ray computed tomography reconstruction of ceramic layers and portions of the metal supports near the ceramic/metal interface. (a) Reproduced with permission from Ref. [24].

with 24 keV X-ray. Dark field images were collected to deduct detector dark counts with the X-ray shutter closed, and bright field images were collected before and after the sample scan to normalize for variations in the incident illumination. The 3D reconstructions were performed with TomoPy, and visualization and image were analyzed with Avizo software. A cell was mounted in epoxy, cut, and polished to prepare for scanning electron microscope (SEM, JEOL JSM-7500F) cross section imaging.

3. Results and discussion

Cell size was scaled up to 50 cm^2 active area, and the manufacturability of the infiltration techniques was improved by using a sprayable low-viscosity aqueous precursor solution and very fast thermal process to convert the precursor to final catalyst compositions.

3.1. Cell size scale-up

The MS-SOFC architecture and processing can be effectively scaled up from button cell size to a larger format with cell size on the order anticipated to be used in a full-size stack. LBNL's symmetric MS-SOFC architecture was previously demonstrated with round button cells (approximately 5–8 cm^2) and rectangular cells (14 cm^2) [18–22,24–30]. Here, small (3 cm^2), medium (8 cm^2), and large (50 cm^2) planar cells were produced using identical fabrication techniques, Fig. 2. The 50 cm^2 cell is the largest that could be produced with existing equipment at LBNL, and is constrained by the size of the hot zone in the sintering furnace using a 10 cm outer diameter controlled-atmosphere tube. Rectangular cells (14 cm^2) were previously sintered successfully in an industrial-scale vacuum/reducing furnace with an approximately 2 m diameter chamber, indicating furnace size is not a constrain on cell size [27–29]. All other cell fabrication processes are anticipated to easily scale up to even larger sizes well above 50 cm^2, including tape casting, laminating, air debinding, and catalyst precursor ink spraying.

The cells were operated with air and humidified hydrogen to demonstrate that the performance is similar for all cell sizes. Operation occurred at isothermal and low fuel utilization conditions, to focus on the impact of cell size and avoid complications from temperature and fuel composition variations that are expected to occur in an operating stack. For the 50 cm^2 cell, nearly isothermal conditions were achieved. The temperature difference between the anode and cathode side was approximately 2 °C, and across the cathode area was approximately 4 °C, Fig. S2. The performance of all cell sizes is nearly identical, Fig. 3. Clearly, the cell fabrication techniques are scalable across a wide range of cell size. Three different 50 cm^2 cells provided reproducible performance, Fig. S3. The cell performance for all cell sizes is lower than previously reported, because the active area of some previous button cells was under-estimated. This error occurred in several recent publications [18–22,24,26,30], but not in earlier or the most recent work [23,25,27–29,31–35]. This is discussed in detail in the Supplementary Information.

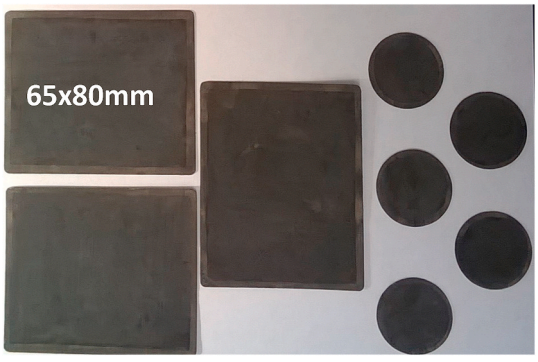

Fig. 2. Cell size scale up. Button cells (8 cm^2) and large cells (50 cm^2) after catalyst deposition. A small perimeter area is masked before catalyst infiltration, which is later covered by glass seal, so the active cell areas reported are slightly smaller than the full cell geometric area.

Key operational benefits of MS-SOFCs include tolerance to thermal cycling and redox cycling [1–4], which were demonstrated for LBNL button cells previously [22,26,30–33]. To demonstrate that these benefits persist for larger cell size, a 50 cm^2 cell was subjected to deep redox cycling and multiple thermal cycles from <100 to 700 °C, Fig. 4. The cell performance and seal integrity were maintained despite this aggressive operation.

3.2. Manufacturability

Previous infiltration of LBNL's MS-SOFCs was carried out *via* a molten salt technique [21,23]. This technique was developed to sustain a high concentration of metal ions in the infiltrant, thus enabling high loading of the catalyst in the electrode pores after only a few, or even a single, infiltration cycle [36–38]. Nitrate salts of the desired metal ions are mixed with a surfactant and melted at a temperature between 65 and 100 °C, depending on the composition of the mixture. In some cases, a very small amount of water is added to assist dissolution (e.g. Sr-nitrate), or prevent decomposition due to overheating (e.g. Mn-nitrate). Because of the negligible water content, the total concentration of metal ions in the melt is very high (~4 M). The MS-SOFC is pre-heated to the melt temperature, and submerged in the melt to introduce the melt into the pores. While effective, this technique has a number of limitations that make it difficult to transition from lab scale to a manufacturing environment. The cells and nitrate melt must be maintained at the correct temperature. Upon cooling, the nitrate melt solidifies and is very difficult to remove from equipment and tools, making it a messy process. The viscosity of the melt is quite high, and varies considerably with temperature, making it difficult to mix and pump. The metal ion concentration in the melt constantly changes due to evaporation of water of crystallization in the hydrated nitrate salt reagents, and the added water. Finally, the melt is unstable and easily overheated to decomposition, and therefore a fresh batch must be made daily.

To improve the manufacturability of the MS-SOFC processing, an aqueous nitrate solution was implemented as the catalyst precursor infiltrant, similar to most previous SOFC infiltration efforts [38,39]. By adding water to the nitrate mixture, a low-viscosity liquid is achieved. The solution is shelf-stable for months, and can be applied to the cell with a number of scalable techniques including aerosol spraying, dip coating, syringe dropping, or brush painting. Here, a hand-held artist's aerosol spray brush was used, but previous work suggests that an ultrasonic robotic spray head or inkjet printing head can easily be used in a manufacturing environment [40–42]. Addition of water does reduce the metal ion concentration somewhat, but only one additional infiltration cycle on each electrode is required to match the performance of cells prepared *via* the molten nitrate technique, Fig. 5. We suspect the aqueous solution wets into the porous structure and more easily fills all the pores in the electrode compared to the molten nitrate liquid.

An alternative faster infiltration processing technique was implemented to greatly increase the throughput of the infiltration process, and we envision continuous processing with a belt furnace in a manufacturing environment. Conversion of the nitrate salt to the desired oxide catalyst composition is accomplished by heating the infiltrated cell in air. LBNL's typical "slow" protocol is heating to 600 or 850 °C with a ramp rate of 3 °C min^{-1}, followed by natural furnace cooling [20,21,24]. This process takes approximately 5–7 h, so only 1 or 2 infiltration cycles can be accomplished in a single work shift. This process was developed with anode-supported and electrolyte-supported cells, and the slow ramp rate was chosen to prevent thermal shock. Because the MS-SOFC architecture can tolerate extremely rapid thermal cycling [30], however, the cells can be heated from room temperature to the final processing temperature within seconds. This "fast" process is

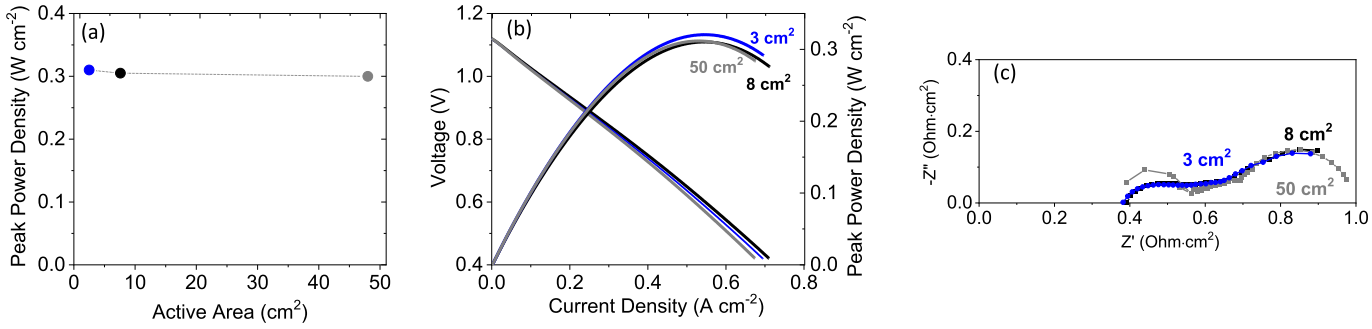

Fig. 3. Cell size scale-up. (a) Peak power density, (b) polarization curves, and (c) EIS spectra at open circuit at 700 °C with air and humidified hydrogen for cells of 3 (blue), 8 (black) and 50 (gray) cm^2 active area. Catalyst precursor solutions were applied by spray deposition. (For interpretation of the references to colour in this figure legend, the reader is referred to the Web version of this article.)

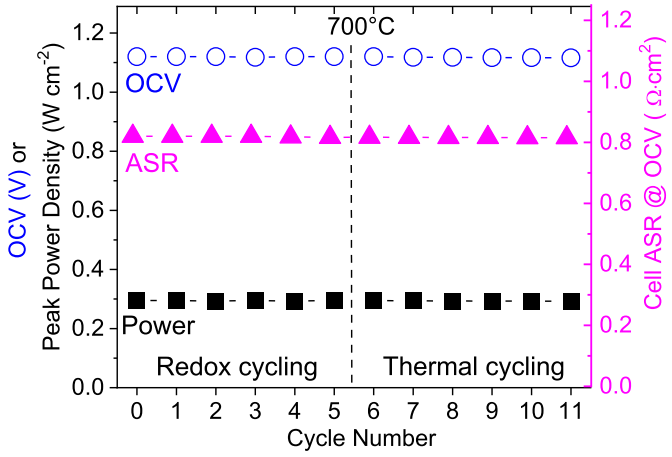

Fig. 4. Tolerance to redox and thermal cycling. Five cycles of full redox cycling (switching the anode gas between air and humidified hydrogen) were followed by six thermal cycles from <100 to 700 °C.

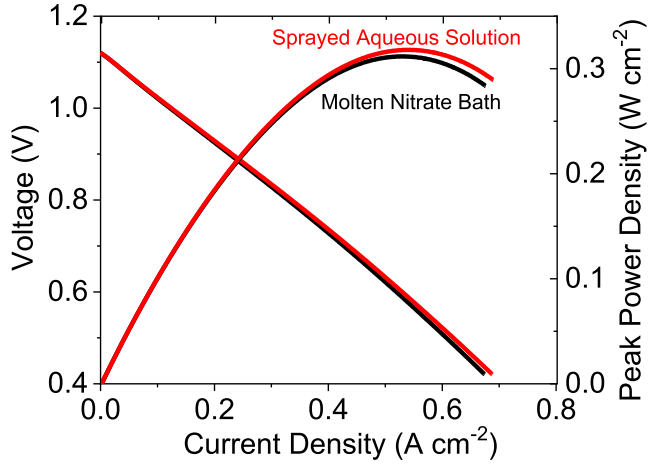

Fig. 5. Comparison of infiltration techniques for Pr-oxide and SDCN catalysts. Performance of 50 cm^2 cells at 700 °C with air and humidified hydrogen prepared *via* (black) molten nitrate infiltration (3 cycles on cathode, 4 cycles on anode) or (red) sprayed aqueous solution infiltration (4 cycles on cathode, 5 cycles on anode). (For interpretation of the references to colour in this figure legend, the reader is referred to the Web version of this article.)

accomplished at the lab scale by placing the infiltrated cells quickly into a pre-heated furnace held at 500 °C, waiting 10 min for the conversion reaction to occur, and then removing the cells from the furnace and cooling in ambient air. The expected catalyst phases are obtained (see Supplementary Fig. S8). The thermal process takes a few minutes, and an entire infiltration cycle including cell preparation, catalyst precursor deposition, and removal of excess catalyst after conversion can be accomplished in an hour.

Using the fast infiltration protocol, many cycles can occur in a single work shift, making it more practical to infiltrate the cell many times. Building up a high loading of well-connected catalyst particles can improve performance and stability [43–45]. Cells were fabricated with between 5 and 20 fast infiltration cycles, and compared to a baseline cell with 5 slow infiltration cycles, Fig. 6. Note that the fast infiltrations took 0.5 to 2 work shifts total for each cell, whereas the slow infiltration took 5 days. The performance of the fast and slow cells with 5 infiltration cycles is similar, Fig. 6a. The initial slope of the I–V curve is similar. At higher current density, the polarization of the slow infiltrated cell increases rapidly, suggesting a mass transport limitation. We presume the rapid nitrate to oxide conversion reaction during fast infiltration removes excess catalyst from the pores of the metal support, thereby improving mass transport in the support. This is supported by the weight gain after catalyst addition *via* slow infiltration being roughly 2.5 times higher than the weight gain after fast infiltration (see Supplementary Fig. S9). For 10 and 15 fast infiltrations, the I–V curves are fairly linear, and the performance is improved by the additional catalyst loading. For 20 fast infiltrations, the performance is limited by mass transport limitation, presumably due to filling of the pores with too much catalyst. Increasing the catalyst loading generally improves the ohmic and polarization impedances, suggesting that catalyst loading as well as electronic and ionic conductivity in the infiltrated catalyst coating are significant factors for cell performance, Figs. 6b and S10. After implementing the improved infiltration process with additional cycles, the peak power density was increased from 0.3 W cm^{-2} for 5 cycles of slow infiltration (Fig. 3) to 0.52 W cm^{-2} for 10 cycles of the fast infiltration process. Coarsening the catalysts by heating to 50 °C above the operating temperature before long-term operation was previously reported to increase durability at the expense of initial performance [19]. Coarsening reduces the performance for the fast infiltrated catalysts as well, Fig. 6c. The impact is lower for 20 cycles, because the mass transport limits the peak power. From these results, it appears the optimum catalyst loading level occurs around the range of 10–15 fast infiltration cycles. Long-term operation will be reported in the future.

Manufacturability is also improved by the symmetric architecture of the cell, Fig. 1. Because the cell structure is completely symmetric during sintering, the cell remains flat and does not warp due to small differences in the metal and ceramic layers' thermal expansion, debinding rate, or sintering rate. An example is shown in Fig. 7. An asymmetric structure

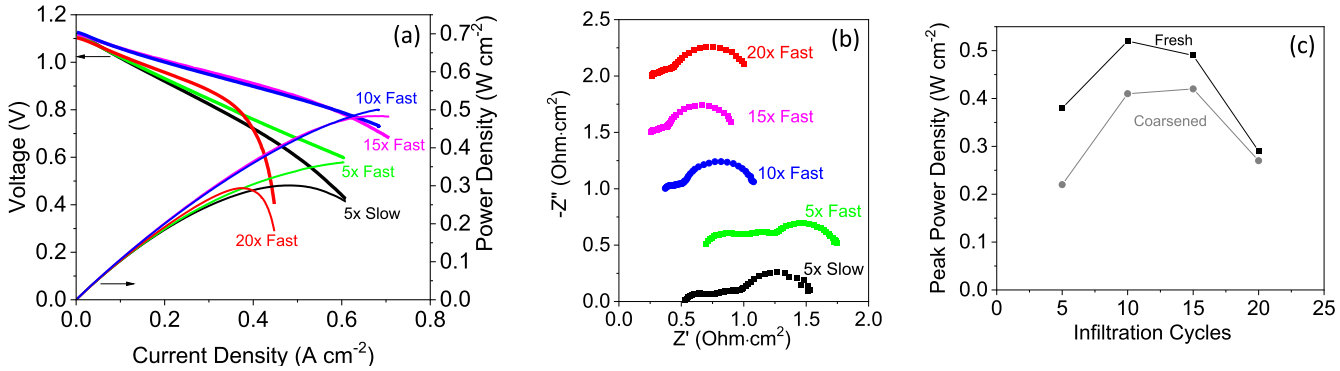

Fig. 6. Comparison of fast and slow infiltration. (a) Initial performance and (b) EIS at open circuit, with air and humidified hydrogen at 700 °C. The number of infiltration cycles indicated in the figures were applied to both the anode and cathode. The EIS spectra were obtained after a temperature excursion to 750 °C for 4 h to coarsen the catalysts, and are offset from the horizontal axis by multiples of 0.5 Ohm*cm^2 for clarity. (c) Peak power density for fast infiltrated cells, before (black squares) and after (gray circles) the temperature excursion.

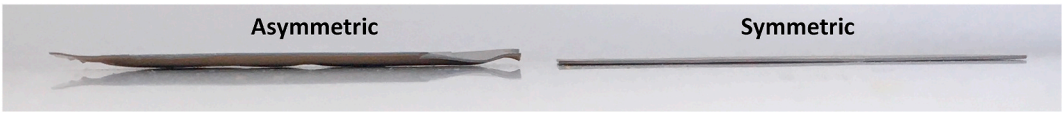

Fig. 7. Symmetric cells are flat. Edge-on photograph of 50 cm^2 (left) asymmetric cell (metal/porous ceramic/dense ceramic/porous ceramic) and (right) symmetric cell (metal/porous ceramic/dense ceramic/porous ceramic/metal) after identical sintering processing.

(one metal layer missing) with minor mismatch between the ceramic and metal layer sintering rates shows significant warping after sintering. Typical shrinkage after sintering at 1350 °C is 21% for the ceramic and 25% for free-standing metal [20]. When co-sintered, the metal shrinkage is somewhat constrained by the adjacent ceramic layer. A symmetric cell prepared from the exact same powders and tapes was flat after sintering. While mismatch between the layers can cause stress during debinding and early-stage sintering, we presume that this stress is removed *via* creep and mechanical sintering shrinkage during the high-temperature sintering hold at 1350 °C. Asymmetry is introduced when the catalysts are deposited, but this process occurs at low temperature (<850 °C) and the catalysts are not part of the mechanical backbone of the cell, so the cell remains flat during the catalyst infiltration process.

Debinding and sintering rates can be sensitive to particle morphology, particle size distribution, and the extent of mixing of solids, poreformers, and binders. These properties may change from lot to lot of ceramic, metal, and poreformer powders used to form the layers, and from batch to batch of slurry used for tape casting. In a manufacturing environment for conventional asymmetric SOFCs, each powder lot and slurry batch must be analyzed and small modifications to the slurry formulations must be made to maintain good matching between adjacent layers and ensure flat cells. In contrast, with a symmetric structured cell, small variations in powder and slurry properties can be accommodated without warping. This is expected to save cost on powder quality control and slurry formulation efforts.

4. Conclusions

The symmetric-structure MS-SOFC was scaled up to 50 cm^2 active area. The cell size was limited by the size of the laboratory sintering furnace, and much larger cell size is anticipated to be viable. Nearly identical performance was achieved for the large cell and button cells produced with the same techniques. Alternative infiltration techniques were developed, and are expected to be more suitable for large-scale manufacturing than LBNL's previous molten salt technique. In particular, an aqueous solution of nitrate salts that can be applied by spray deposition was implemented. It appears the technique used to deposit the nitrate salts is not critical for performance, as long as the pores are filled. A very fast ramp thermal conversion step was used to dramatically decrease the infiltration processing time and permits many infiltration cycles to be conducted in a single work shift. The symmetric MS-SOFC architecture enables this very fast thermal processing, and also maintains cell flatness during debinding and sintering, even if perfect shrinkage matching between the ceramic and metal layers is not achieved. The large cell size demonstration and processing improvements reported here are a critical milestone on the path of scaling up LBNL's MS-SOFC design from lab scale to a manufacturing environment.

CRediT authorship contribution statement

Emir Dogdibegovic: Investigation, Visualization. **Yuan Cheng:** Investigation, Visualization. **Fengyu Shen:** Investigation, Visualization. **Ruofan Wang:** Investigation. **Boxun Hu:** Investigation, Visualization. **Michael C. Tucker:** Conceptualization, Investigation, Writing - original draft, Supervision, Funding acquisition.

Declaration of competing interest

The authors declare that they have no known competing financial interests or personal relationships that could have appeared to influence the work reported in this paper.

Acknowledgements

We are grateful to Dr. Dula Parkinson for help with microtomography measurement at Beamline 8.3.2 of Advanced Light Source (ALS). Grace Lau assisted with cell preparation. The information, data, or work presented herein was funded in part by the Advanced Research Projects Agency - Energy, U.S. Department of Energy under work authorization number 18/CJ000/04/01. This work was funded in part by the U.S. Department of Energy Technology Commercialization Fund under project TCF-18-15740. This research used resources of the Advanced Light Source, a DOE Office of Science User Facility under contract no. DE-AC02-05CH11231. The authors gratefully acknowledge

research support from the HydroGEN Advanced Water Splitting Materials Consortium, established as part of the Energy Materials Network under the U.S. Department of Energy, Office of Energy Efficiency and Renewable Energy, Fuel Cell Technologies Office, under Contract Number DE-AC02-05CH11231. This work was funded in part by the U.S. Department of Energy under contract no. DE-AC02-05CH11231. We thank Nissan Motor Co., Ltd. and Nissan Technical Center North America for providing cost share and helpful discussion. The views and opinions of the authors expressed herein do not necessarily state or reflect those of the United States Government or any agency thereof. Neither the United States Government nor any agency thereof, nor any of their employees, makes any warranty, expressed or implied, or assumes any legal liability or responsibility for the accuracy, completeness, or usefulness of any information, apparatus, product, or process disclosed, or represents that its use would not infringe privately owned rights.

Appendix A. Supplementary data

Supplementary data to this article can be found online at https://doi.org/10.1016/j.jpowsour.2020.229439.

References

[1] A.M. Dayaghi, K.J. Kim, S. Kim, J. Park, S.J. Kim, B.H. Park, G.M. Choi, J. Power Sources 324 (2016) 288–293.
[2] V.V. Krishnan, Wiley Interdiscipl. Rev.: Energy Environ. 6 (2017) 246.
[3] Y. Larring, M.-L. Fontaine, (2013) 71-93.
[4] M.C. Tucker, J. Power Sources 195 (2010) 4570–4582.
[5] R.T. Leah, A. Bone, A. Selcuk, M. Rahman, A. Clare, M. Lankin, F. Felix, S. Mukerjee, M. Selby, ECS Trans. 91 (2019) 51–61.
[6] M.C. Tucker, Int. J. Hydrogen Energy 45 (2020) 24203–24218.
[7] M. Stange, E. Stefan, C. Denonville, Y. Larring, P.M. Rørvik, R. Haugsrud, Int. J. Hydrogen Energy 42 (2017) 13454–13462.
[8] E. Stefan, M. Stange, C. Denonville, Y. Larring, N. Hildenbrand, T. Norby, R. Haugsrud, J. Mater. Sci. 52 (2017) 6486–6497.
[9] T. Franco, K. Schibinger, Z. Ilhan, G. Schiller, A. Venskutonis, ECS Trans. 7 (2007) 771–780.
[10] R. Hui, Z. Wang, O. Kesler, L. Rose, J. Jankovic, S. Yick, R. Maric, D. Ghosh, J. Power Sources 170 (2007) 308–323.
[11] D. Udomsilp, J. Rechberger, R. Neubauer, C. Bischof, F. Thaler, W. Schafbauer, N. H. Menzler, L.G.J. de Haart, A. Nenning, A.K. Opitz, O. Guillon, M. Bram, Cell Rep. Phys. Sci. 1 (2020) 100072.
[12] P. Blennow, J. Hjelm, T. Klemensø, A.s. Persson, K. Brodersen, A. Srivastava, H. Frandsen, M. Lundberg, S. Ramousse, M. Mogensen, ECS Trans. 25 (2009) 701.
[13] T. Chen, Y. Zhou, M. Liu, C. Yuan, X. Ye, Z. Zhan, S. Wang, Electrochem. Commun. 54 (2015) 23–27.
[14] Y. Zhou, C. Yuan, T. Chen, X. Meng, X. Ye, J. Li, S. Wang, Z. Zhan, J. Power Sources 267 (2014) 117–122.
[15] A. Hagen, A.C. Wulff, P. Zielke, X. Sun, B. Talic, I. Ritucci, H.L. Frandsen, S. H. Jensen, W.R. Kiebach, P.V. Hendriksen, Int. J. Hydrogen Energy 45 (2020) 29201–29211.
[16] G. Schiller, A. Ansar, M. Lang, O. Patz, J. Appl. Electrochem. 39 (2009) 293–301.
[17] A. Nechache, F. Han, R. Semerad, G. Schiller, R. Costa, ECS Trans. 78 (2017) 3039–3047.
[18] E. Dogdibegovic, Y. Fukuyama, M.C. Tucker, J. Power Sources 449 (2020) 227598.
[19] E. Dogdibegovic, R. Wang, G.Y. Lau, A. Karimaghaloo, M.H. Lee, M.C. Tucker, J. Power Sources 437 (2019) 226935.
[20] E. Dogdibegovic, R. Wang, G.Y. Lau, M.C. Tucker, J. Power Sources 410–411 (2019) 91–98.
[21] M.C. Tucker, Energy Technol. 5 (2017) 2175–2181.
[22] M.C. Tucker, J. Power Sources 369 (2017) 6–12.
[23] M.C. Tucker, G.Y. Lau, C.P. Jacobson, L.C. DeJonghe, S.J. Visco, J. Power Sources 171 (2007) 477–482.
[24] R. Wang, E. Dogdibegovic, G.Y. Lau, M.C. Tucker, Energy Technol. 7 (2019) 1801154.
[25] F. Shen, R. Wang, M.C. Tucker, J. Power Sources 474 (2020) 228618.
[26] M.C. Tucker, J. Power Sources 395 (2018) 314–317.
[27] M.C. Tucker, B. Carreon, J. Charyasatit, K. Langston, C. Taylor, J. Manjarrez, N. Burton, M. LaBarbera, C.P. Jacobson, ECS Trans. 57 (2013) 503–509.
[28] M.C. Tucker, B. Carreon, J. Charyasatit, K. Langston, C. Taylor, J. Manjarrez, N. Burton, M. LaBarbera, C.P. Jacobson, ECS Trans. 78 (2017) 229–236.
[29] M.C. Tucker, C. Taylor, M. LaBarbera, C.P. Jacobson, ECS Trans. 57 (2013) 2929–2937.
[30] M.C. Tucker, A.S. Ying, Int. J. Hydrogen Energy 42 (2017) 24426–24434.
[31] M.C. Tucker, Int. J. Hydrogen Energy 43 (2018) 8991–8998.
[32] M.C. Tucker, C.P. Jacobson, L.C. De Jonghe, S.J. Visco, J. Power Sources 160 (2006) 1049–1057.
[33] M.C. Tucker, G.Y. Lau, C.P. Jacobson, L.C. DeJonghe, S.J. Visco, J. Power Sources 175 (2008) 447–451.
[34] M.C. Tucker, G.Y. Lau, C.P. Jacobson, S.J. Visco, L.C. De Jonghe, J. Power Sources 195 (2010) 3119–3123.
[35] R. Wang, C. Byrne, M.C. Tucker, Solid State Ionics 332 (2019) 25–33.
[36] Y. Huang, J.M. Vohs, R.J. Gorte, Electrochem. Solid State Lett. 9 (2006) A237–A240.
[37] T.Z. Sholklapper, C. Lu, C.P. Jacobson, S.J. Visco, L.C. De Jonghe, Electrochem. Solid State Lett. 9 (2006) A376–A378.
[38] T.Z. Sholklapper, C.P. Jacobson, S.J. Visco, L.C. De Jonghe, Fuel Cell. 8 (2008) 303–312.
[39] S.P. Jiang, Int. J. Hydrogen Energy 37 (2012) 449–470.
[40] R.P. Dowd, S. Lee, Y. Fan, K. Gerdes, Int. J. Hydrogen Energy 41 (2016) 14971–14981.
[41] T. Hong, S. Lee, P. Ohodnicki, K. Brinkman, Int. J. Hydrogen Energy 42 (2017) 24978–24988.
[42] T.B. Mitchell-Williams, R.I. Tomov, S.A. Saadabadi, M. Krauz, P.V. Aravind, B. A. Glowacki, R.V. Kumar, Mater. Renew. Sustain. Energy 6 (2017) 12.
[43] J. Ju, Y. Xie, Z. Wang, Y. Zhang, C. Xia, J. Electrochem. Soc. 163 (2016) F393–F400.
[44] J.M. Vohs, R.J. Gorte, Adv. Mater. 21 (2009) 943–956.
[45] A.J. Samson, P. Hjalmarsson, M. Søgaard, J. Hjelm, N. Bonanos, J. Power Sources 216 (2012) 124–130.